Research Square

Preprints are preliminary reports that have not undergone peer review.
They should not be considered conclusive, used to inform clinical practice,
or referenced by the media as validated information.

Estimation of the State of Power for lithium-ion batteries based on an improved asymmetric polarization model

Yingyang Wu
Inner Mongolia University of Technology
Yonggang Yue
Inner Mongolia University of Technology
Shunli Wang
497420789@qq.com
Inner Mongolia University of Technology
Qin Zhang
Inner Mongolia University of Technology
Fernandez Carlos
Inner Mongolia University of Technology

Research Article

Keywords: Lithium-ion battery, State of power estimation, Kalman filter, equivalent model, multi-constraint estimation

Posted Date: May 5th, 2026

DOI: https://doi.org/10.21203/rs.3.rs-9038085/v1

License: This work is licensed under a Creative Commons Attribution 4.0 International License.
Read Full License

Additional Declarations: No competing interests reported.

Estimation of the State of Power for lithium-ion batteries based on an improved asymmetric polarization model

Yingyang Wu[1, 2], Yonggang Yue[1], Shunli Wang[1, 3*], Zhang Qin[1, 2], Carlos Fernandez[4]

1 Electric Power College, Inner Mongolia University of Technology, Inner Mongolia 010000, China; 2 School of Information Engineering, Southwest University of Science and Technology, Mianyang 621010, China; 3 School of Information Technology, Urban Vocational College of Sichuan, Chengdu 610000, China; 4 School of Pharmacy and Life Sciences, Robert Gordon University, Aberdeen AB10-7GJ, UK.

*Corresponding author(s). E-mail(s): 497420789@qq.com.

***Abstract*—Accurate state of power (SOP) estimation is essential for the safe and reliable operation of lithium-ion battery management systems. The present study proposes a high-precision SOP estimation framework based on an Firefly Asymmetric Polarization-Adaptive Extended Kalman Filter (FAP-AEKF) integrated with an improved second-order resistance–capacitance partnership for a new generation of vehicle (RC-PNGV) model. To characterize the asymmetric polarization behavior during charging and discharging, a bidirectional diode–resistance network and an additional polarization capacitor branch are introduced into the conventional model. An FAP, incorporating parallel computing, adaptive step-size attenuation, normalized distance, and elite retention strategies, is employed to achieve high-precision offline parameter identification. In contrast, the AEKF performs robust online estimation of the state of charge and terminal voltage under time-varying noise conditions. Based on this, a multi-constraint SOP estimation framework is established for multi-time-scale peak power prediction, considering voltage, current, and state-of-charge limits. Experimental results obtained under three working conditions, spanning temperatures from 15℃ to 35℃, demonstrate voltage root-mean-square errors of less than 0.01 mV, state of charge (SOC) errors of within 2.80%, and average power estimation errors of less than 30 W, confirming the accuracy and robustness of the proposed FAP-AEKF-based SOP estimation method.**

Keywords: Lithium-ion battery; State of power estimation; Kalman filter; equivalent model; multi-constraint estimation.

1 Introduction

1.1 Background and significance of the research

With the rapid development of new energy vehicles, lithium-ion batteries have become the core power source of electric vehicles. The SOP of the battery is a key indicator for the battery management system to achieve safe control and performance optimization, and its accurate estimation highly depends on a reasonable battery model and an efficient estimation algorithm[1-4]. Therefore, constructing a high-precision and robust SOP estimation method is of great engineering significance for ensuring the safe and reliable operation of batteries.

1.2 Current research status of the subject

1.2.1 Research Status of SOP State Estimation

Currently, academic research pertaining to battery SOP estimation is continuously advancing in terms of accuracy improvement, adaptability to complex operating conditions, and real-time performance optimization, gradually forming three technical paths: model-driven, data-driven, and hybrid-driven[5-12]. In the past three years, related research has shown a trend of multi-method integration and multi-factor coupling, emphasizing the precise characterization and rapid response of battery dynamic characteristics in complex operating environments.

In the model-driven field, research focuses on optimizing model structure and enhancing parameter adaptive capabilities[13,14]. In 2025, Sidi Dong proposed a partially adaptive fractional-order multi-cell model

(PA-FOM-MCM), which effectively mitigated the consistency issue of battery packs by combining a two-stage algorithm, reducing the root mean square error (RMSE) of SOP estimation by 52.55% and achieving a single run time of only 0.0298 seconds, meeting the requirements of on-board real-time applications[15]. In 2024, Ying Liu et al. proposed a method based on an electrothermal coupling model combined with multi-innovation unscented Kalman filtering, achieving joint estimation of SOC/SOP across the entire SOC range in a wide temperature range, with RMSE controlled within 3%[16-19]. Meanwhile, data-driven and hybrid-driven methods have developed rapidly. Xueyi Hao's DWPSO-optimized LSSVM-PF method reduced the average absolute error by approximately 35% within the range of -10℃ to 45℃. The physical information fusion framework, by integrating simplified electrochemical models with Gaussian process regression, significantly improved computational efficiency while maintaining accuracy[20-22]. Although deep learning methods such as LSTM and GRU have potential, their overall accuracy is still slightly inferior to that of hybrid-driven methods.

Overall, model-driven methods, due to their clear mechanisms and high reliability, still dominate in engineering applications, while data-driven and hybrid-driven methods have achieved accuracy breakthroughs by leveraging nonlinear modeling advantages[23-26]. However, existing research still has deficiencies in extreme temperature adaptability, asymmetric polarization characteristics, and dynamic optimization under multiple constraints[27-29]. Future research will focus more on the collaborative design of "mechanism model optimization - intelligent algorithm improvement - multi-constraint coupling", achieving high-precision and high-real-time SOP estimation through the deep integration of the three[30-33].

1.2.2 Research Work of This Paper

The present study focuses on high-precision SOP estimation of a ternary lithium-ion battery. Based on capacity calibration and Hybrid Pulse Power Characterization (HPPC) data under complex multi-temperature conditions, the limitations of the traditional second-order RC-PNGV model were analyzed. Specifically, to address the difficulty in characterizing asymmetric polarization during charging and discharging, a bidirectional resistance-diode structure is introduced to improve the model[34-39]. On this basis, the firefly optimization algorithm with adaptive step size is adopted to achieve high-precision identification of model parameters, and the adaptive extended Kalman filter is combined to complete the robust online estimation of SOC and terminal voltage[40-45]. Further, a SOP estimation framework with coordinated constraints of voltage, current, and SOC is constructed, forming a SOP estimation method system that is both physically consistent and practically useful. The research process is shown in Figure 1.

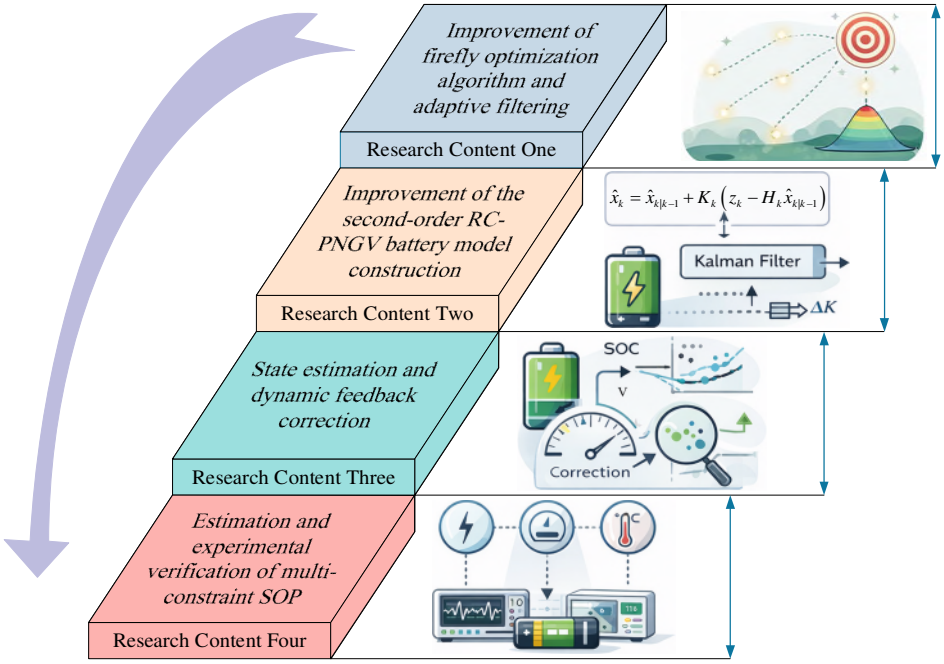


Figure 1. Research Process of Multi-constraint Estimation for Lithium-ion Battery SOP

Figure 1 presents the overall research process of this study: an improved RC-PNGV model is established based on experimental data, and state estimation is achieved by combining the improved firefly algorithm with adaptive extended Kalman filtering. Moreover, multi-time-scale SOP prediction is completed under multiple constraints.

2 Theoretical analysis

Based on literature review and experimental analysis, this study improves the traditional second-order RC-PNGV model by introducing a diode–resistance parallel network to describe asymmetric charging and discharging characteristics and adding an RC parallel branch to represent the battery's dynamic and static responses. On this basis, by integrating parallel computing, adaptive step size attenuation, distance normalization, and optimal attractor selection strategies, an improved firefly optimization algorithm is constructed to achieve efficient and high-precision identification of model parameters. Further, by combining adaptive extended Kalman filtering, the stability and physical consistency of SOC and terminal voltage estimation are enhanced. Ultimately, high-precision estimation of multi-time-scale SOP is achieved under multiple constraints of voltage, current, and SOC.

2.1 The improved second-order RC-PNGV model

2.1.1 Analysis of Working Characteristics of Lithium-ion Batteries with a Ternary Material

Lithium-ion batteries with a ternary cathode have been widely applied in the field of new energy vehicles due to their outstanding advantages, such as high energy density, low pollution, and long cycle life. Specifically, compared with lithium iron phosphate batteries, ternary lithium-ion batteries not only have higher energy density but also perform better in low-temperature environments. Figure 2 shows the schematic diagram of the principle of lithium-ion batteries during the charging and discharging process.

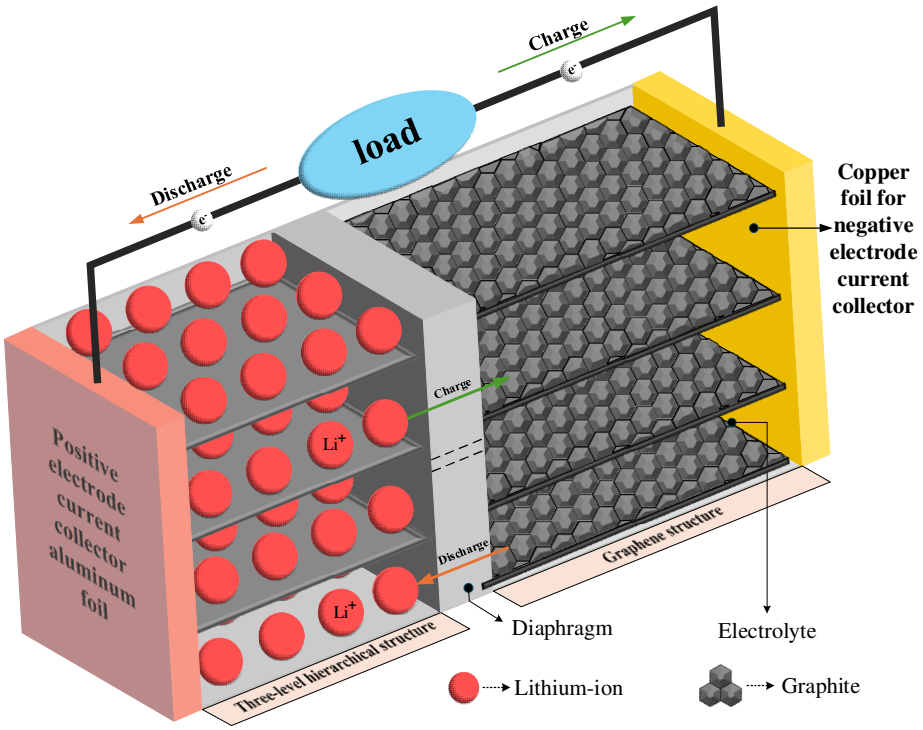


Figure 2. The working principle of the internal state of lithium-ion batteries

The ternary lithium-ion battery achieves the intercalation and deintercalation of lithium ions (Li^+) through the layered structure of the positive and negative electrodes. During charging, Li^+ migrates from the positive electrode, passes through the electrolyte, and intercalates into the negative electrode, while electrons move synchronously through the external circuit, converting electrical energy into chemical energy for storage. The discharging process is the opposite, where chemical energy is converted into electrical energy for release. The essence of charging and discharging is the directional migration and recombination of Li^+ and electrons driven by the electric field.

2.1.2 Analysis of the Improved Second-Order RC-PNGV Model

The second-order RC-PNGV model is a classic equivalent circuit model of lithium-ion batteries developed based on the PNGV standard. It consists of an open-circuit voltage source, an ohmic internal resistance, and a two-stage RC parallel network. Specifically, R_1-C_1 and R_2-C_2 respectively represent the short-term and long-term polarization characteristics of the battery, which can describe the dynamic response of the battery at different time scales and provide effective model support for state estimation, such as SOC and SOP.

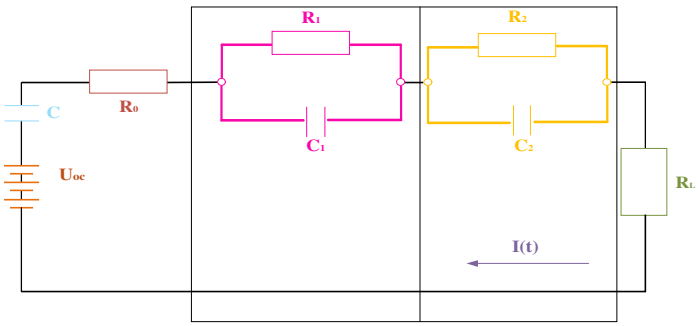


Figure 3. Second-order RC-PNGV model

The second-order RC-PNGV model characterizes the polarization effects at different time scales through two RC branches and has better dynamic response capability than the first-order model under variable current conditions. However, in SOP estimation, its description of the strong nonlinearity of the open circuit voltage (OCV)-SOC relationship and the time-varying nature of polarization parameters is still insufficient, especially prone to introducing boundary errors under conditions of high and low SOC, temperature changes, and deep cycling. Therefore, an improved second-order RC-PNGV model is developed to more accurately capture the dynamic characteristics of the charging and discharging process of ternary lithium-ion batteries. Its structure is shown in Figure 4.

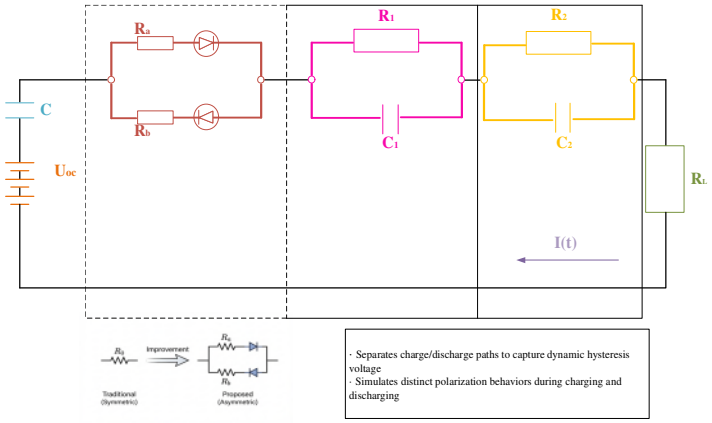


Figure 4. The improved second-order RC-PNGV model

The improved second-order RC-PNGV model, based on the traditional second-order RC-PNGV model, adds a parallel branch composed of a forward diode R_a and a reverse diode R_b. Through the unidirectional conductivity of the diodes, it realizes the differentiated characterization of the polarization reaction during the charging and discharging processes.

The improved second-order RC-PNGV model adds a polarization resistance branch controlled by a diode on the basis of the traditional model: R_a is on during discharge, and R_b is on during charge, thereby depicting the asymmetric polarization characteristics of charging and discharging. The model characterizes the polarization dynamics at different time scales through the R_1-C_1 and R_2-C_2 networks, and combines the ohmic internal resistance is R_a/R_b and the open-circuit voltage source U_{oc} to construct a state equation that can distinguish the charging and discharging processes, providing an accurate equivalent circuit basis for subsequent SOC calculation and SOP estimation.

$$\begin{cases} i_{p1}(t)=\dfrac{U_{p1}(t)}{R_1}+C_1\dfrac{\mathrm{d}U_{p1}(t)}{\mathrm{d}t} \\ i_{p2}(t)=\dfrac{U_{p2}(t)}{R_2}+C_2\dfrac{\mathrm{d}U_{p2}(t)}{\mathrm{d}t} \\ \dfrac{\mathrm{d}U_C(t)}{dt}=\dfrac{I_t}{C} \\ \dfrac{\mathrm{d}SOC(t)}{\mathrm{d}t}=-\dfrac{I(t)}{Q_{\mathrm{nom}}} \\ U_L=U_{OC}(SOC)-U_{p1}(t)-U_{p2}(t)-U_c(t)-R_aI(t) \\ I(t)=i_{p1}(t)=i_{p2}(t) \end{cases} \tag{1}$$

$$\begin{cases} i_{p1}(t)=\dfrac{U_{p1}(t)}{R_1}+C_1\dfrac{\mathrm{d}U_{p1}(t)}{\mathrm{d}t} \\ i_{p2}(t)=\dfrac{U_{p2}(t)}{R_2}+C_2\dfrac{\mathrm{d}U_{p2}(t)}{\mathrm{d}t} \\ \dfrac{\mathrm{d}U_C(t)}{dt}=\dfrac{I_t}{C} \\ \dfrac{\mathrm{d}SOC(t)}{\mathrm{d}t}=\dfrac{I_c(t)}{Q_{\mathrm{nom}}} \\ U_L=U_{OC}(SOC)+U_{p1}(t)+U_{p2}(t)+R_bI_c(t)+U_c(t) \\ I_c(t)=i_{p1}(t)=i_{p2}(t) \end{cases} \tag{2}$$

Equations (1) and (2) describe the dynamic characteristics of the improved second-order RC-PNGV model under discharging and charging conditions, respectively. The first two equations depict the current balance of the short-period and long-period polarization networks, reflecting the changes in polarization voltage at different time scales. The third equation describes the evolution law of the PNGV branch capacitor voltage U_c. The fourth equation follows the ampere-hour integration method and describes the state evolution of the SOC. The fifth equation is the terminal voltage equation, which reflects the core differences of the model under different operating conditions: during discharging, the terminal voltage U_L is the open-circuit voltage minus the polarization voltage drop, the PNGV capacitor voltage drop, and the voltage drop across the discharging internal resistance R_a; during charging, it is the sum of each voltage term and the open-circuit voltage. The sixth equation satisfies Kirchhoff's current law to achieve current conservation. By introducing separate discharging resistance R_a and charging resistance R_b, this model realizes a refined characterization of the asymmetric polarization characteristics of the battery.In the following equations, $I(t)$ in Eq. (1) represents the discharge current (I>0), while $I_c(t)$ in Eq. (2) represents the absolute magnitude of the charging current ($I_c(t)$=|$I(t)$|). It should be noted that while Eq. (2) uses the current magnitude to explicitly illustrate the voltage rise during charging, the subsequent state-space model (Eq. 14) adopts a unified signed current convention (positive for discharge, negative for charge) to facilitate matrix operations in the Kalman filter.

$$SOC(t)=SOC(t_0)-\frac{1}{Q_{\mathrm{nom}}}\int_{t_0}^{t}\eta(\tau)\cdot I(\tau)\mathrm{d}\tau \tag{3}$$

In formula (3), $SOC(t)$ represents the state of charge at the current time t; $SOC(t_0)$ indicates the SOC at the initial time t_0; Q_{nom}denotes the rated capacity of the battery, which is matched with the current scale in the voltage balance equation of the model; $I(\tau)$ is the working current at time τ; and $\eta(\tau)$ is the Coulombic efficiency.

$$\underbrace{\begin{pmatrix} SOC_{k+1} \\ U_{p1,k+1} \\ U_{p2,k+1} \\ U_{C,k+1} \end{pmatrix}}_{x_{k+1}} = \underbrace{\begin{pmatrix} 1 & 0 & 0 & 0 \\ 0 & \mathrm{e}^{-\Delta t/\tau_1} & 0 & 0 \\ 0 & 0 & \mathrm{e}^{-\Delta t/\tau_2} & 0 \\ 0 & 0 & 0 & 1 \end{pmatrix}}_{\mathrm{A}} \begin{pmatrix} SOC_k \\ U_{p1,k} \\ U_{p2,k} \\ U_{C,k} \end{pmatrix} + \begin{pmatrix} -\dfrac{\eta\Delta t}{Q_n} \\ R_1(1-\mathrm{e}^{-\Delta t/\tau_1}) \\ R_2(1-\mathrm{e}^{-\Delta t/\tau_2}) \\ \dfrac{\Delta t}{C} \end{pmatrix} i_k+\omega_k \tag{4}$$

$$U_k=U_{OC}(SOC_k)-U_{p1,k}-U_{p2,k}-U_{C,k}-R_{\mathrm{pol},k}i_k+v_k \tag{5}$$

In formula (4), x_{k+1} represents the state vector at step k+1, which is composed of the state of charge

SOC_{k+1}, short-term polarization voltage $U_{p1,k+1}$, long-term polarization voltage $U_{p2,k+1}$, and PNGV branch capacitor voltage $U_{C,k+1}$. The state transition matrix A contains exponential terms reflecting the dynamic attenuation characteristics of the RC network, with time constants $\tau_1=R_1C_1$ and $\tau_2=R_2C_2$. i_k is the predicted working current at step k (positive for discharge and negative for charge), and ω_k is the process noise. The control vector includes the term $\frac{\Delta t}{C}$ to represent the evolution law of the capacitor voltage with respect to the current integration. Formula (5) defines the observed variable as the load terminal voltage U_k. This voltage is mapped from the open-circuit voltage $U_{OC}(SOC_k)$ and then reduced by the voltage drops caused by the polarization voltages $U_{p1,k}$ and $U_{p2,k}$, and the charge-discharge polarization resistance $R_{\text{pol},k}$. Here, $R_{\text{pol},k}$ is used to distinguish the asymmetric polarization characteristics (being R_a during discharge and R_b during charge), and v_k represents the observation noise.

2.2 Analysis of Adaptive Mechanism-Driven Firefly Optimization

2.2.1 Analysis of the Traditional Firefly Algorithm

The firefly algorithm (FA) is an optimization algorithm inspired by the natural luminous migration behavior of firefly groups. Its basic principle is that fireflies with lower brightness will move towards those with higher brightness, achieving the search of the solution space through the attraction and movement among the group. The core of the standard FA lies in two concepts: the light intensity of fireflies and their mutual attraction. Figure 5 shows the principal flowchart of the firefly algorithm.

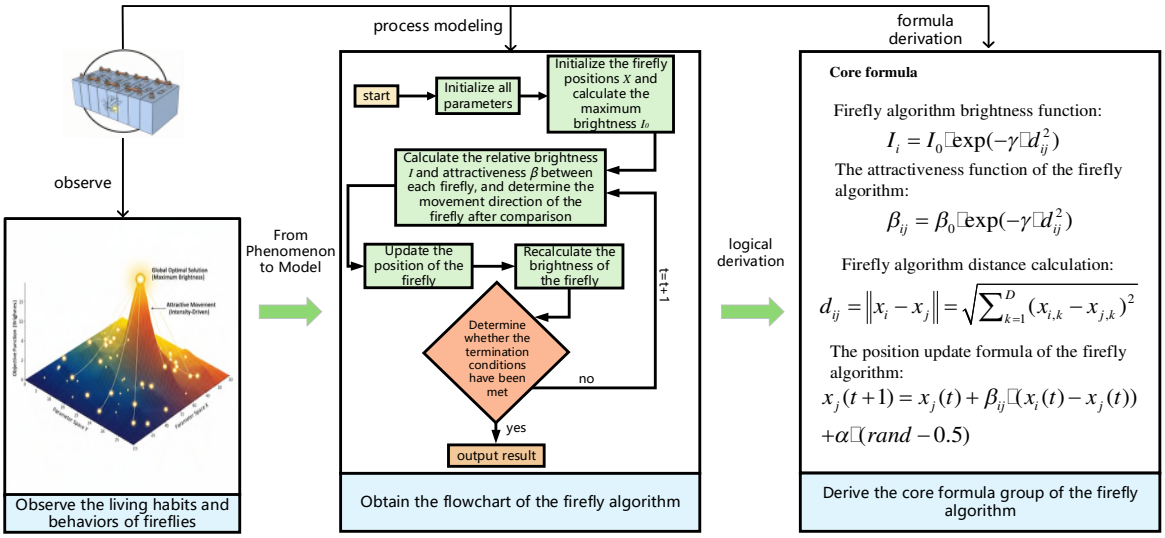


Figure 5. The principle and process of the traditional firefly algorithm

The standard FA is based on the brightness attraction among groups for optimization. However, it has some shortcomings in battery model parameter identification: its serial computing method leads to low computational efficiency in high-dimensional nonlinear problems; the fixed random step size makes it difficult to balance global exploration and local exploitation, which easily leads to local optimum or slow convergence; and the "full attraction" strategy is prone to oscillation in the later stage of iteration, affecting the stability of convergence. These deficiencies limit its application effect in complex battery parameter identification.

2.2.2 Firefly Asymmetric Polarization

In view of the deficiencies of the standard FA in battery parameter identification, the FA is improved from four aspects—parallel computing, adaptive step size, normalized distance, and elite strategy—to significantly enhance the accuracy and efficiency of parameter identification and to provide a reliable model foundation for subsequent precise SOP estimation. Figure 6 shows the principal flowchart of the FAP.

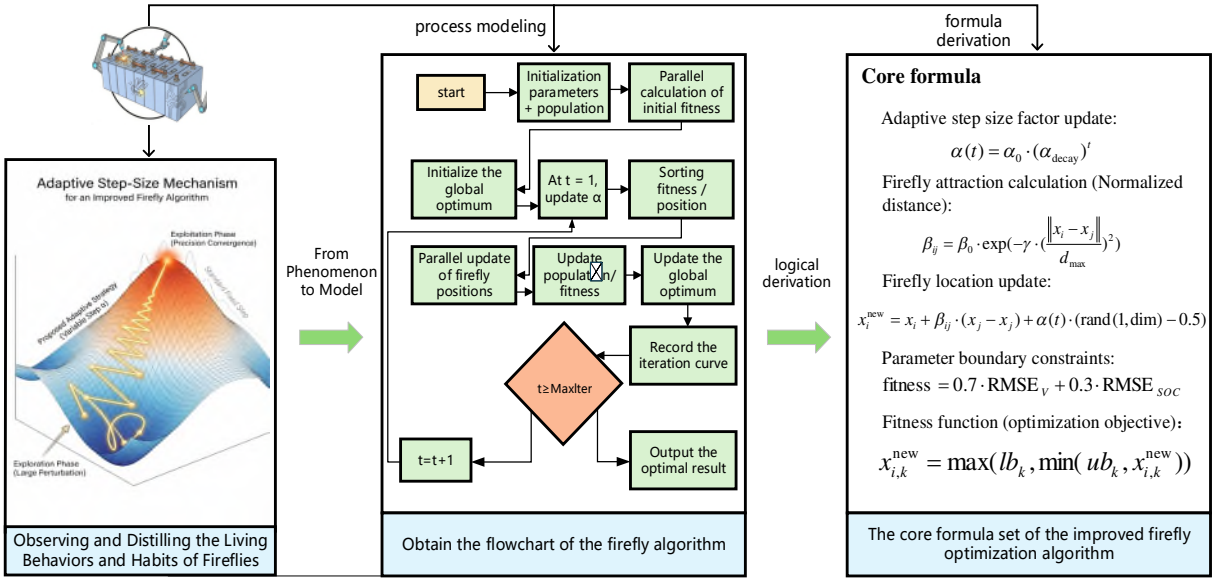


Figure 6. The principle and process of the Adaptive Mechanism-Driven Firefly Optimization

Parallel computing architecture design: To address the issues of complex and time-consuming fitness function calculation in battery model parameter identification, a parallel computing architecture is introduced. Assuming the population size is N, the number of processor cores is P, and the complexity of the fitness function calculation is $O(f)$, the parallelized computing time is reduced from the serial computing time of $T_{\text{serial}}=N\times O(f)$ to the expression in Equation (6).

$$T_{\text{parallel}}=\frac{N\times O(f)}{P}+O_{\text{overhead}} \tag{6}$$

In formula (6), O_{overhead} represents the overhead of parallel communication. This improvement significantly enhances the algorithm's efficiency, allowing for more iterations within a limited time or the use of a larger population size, thereby strengthening the algorithm's global search capability.

Adaptive step size attenuation mechanism: To address the imbalance between exploration and exploitation caused by a fixed step size, an exponentially decaying step size factor was designed, as shown in formula (7).

$$\alpha(t)=\alpha_0\times\delta^t \tag{7}$$

In Equation (7), α_0=0.5 is the initial step size, δ=0.98 is the attenuation factor, and t is the current iteration number. The improved position update formula is (8).

$$x_i^{t+1}=x_i^t+\beta_0 e^{-\gamma r_{ij}^2}(x_j^t-x_i^t)+\alpha_0\delta^t(\text{rand-0.5}) \tag{8}$$

This mechanism enables the algorithm to maintain a larger step size in the early stage of iteration, enhancing the global exploration ability, and adopt a smaller step size in the later stage of iteration, improving the local exploitation accuracy. It effectively balances global search and local optimization.

Normalized distance metric: To eliminate the influence of the different dimensions and numerical ranges of parameters on the algorithm performance, the normalized Euclidean distance, as shown in Equation (9), is adopted.

$$r_{ij}=\frac{\left\|x_i\text{-}x_j\right\|_2}{d_{\max}} \tag{9}$$

In Equation (9), $d_{\max}=\sqrt{\sum_{k=1}^{D}(ub_k\text{-}lb_k)^2}$ represents the maximum diagonal distance of the search space, where D is the dimension of the parameters. The normalized attractiveness is calculated as shown in Equation (10).

$$\beta=\beta_0 e^{-\gamma r_{ij}^2} \tag{10}$$

The normalized distance metric eliminates the differences in the dimensions and scales of different parameters, avoids the dominance of a single dimension in distance calculation, makes the attraction degree between fireflies truly reflect the relative position relationship, and thereby enhances the balance and stability of the search process.

Elite retention strategy: To ensure the information of outstanding individuals is passed on, an elite retention strategy is introduced in each iteration. The population is sorted by fitness according to formula (11).

$$[F_{\text{sorted}},X_{\text{sorted}}]=\text{sort}[Fintess] \tag{11}$$

Retaining the individual with the best fitness in the algorithm prevents the loss of high-quality solutions during random movement, enhancing the convergence stability of the algorithm. In addition to the elite strategy, an optimal attractor selection strategy is implemented. Instead of moving towards all brighter fireflies (standard FA), which causes oscillation, the individual only updates its position towards the single brightest firefly within its perception range in the current iteration. This significantly reduces computational redundancy and improves convergence stability. Meanwhile, precise model parameter identification plays a crucial role in the estimation of multiple constraints of SOP. The high-precision parameters identified by the FAP ensure the reliability of the core calculations in SOP prediction. When calculating the peak current for a continuous L seconds, the prediction accuracy of the terminal voltage constraint equation highly depends on the identified resistance and capacitance parameters, as expressed in Equation (12).

$$U_{T,L}=OCV(SOC)\text{-}I_L\cdot R_a\text{-}U_1e^{-L/\tau_1}\text{-}U_2e^{-L/\tau_2}\text{-}U_c\text{-}I_LR_1(1\text{-}e^{-L/\tau_1})\text{-}I_LR_2(1\text{-}e^{-L/\tau_2})\text{-}\frac{I_L\cdot L}{C}=U_{\lim} \tag{12}$$

In Equation (12), $\tau_1=R_1C_1$ and $\tau_2=R_2C_2$. The high-precision parameters identified by FAP enhance the authenticity of voltage prediction, making the peak current I_L closer to the physical limit. Meanwhile, the precise SOC trajectory strengthens the reliability of SOC constraints, thereby achieving accurate SOP prediction under different durations, providing a reliable basis for battery management system (BMS) power distribution and safety

domain definition.

2.3 Adaptive Extended Kalman Filter Combined with Firefly Asymmetric Polarization

To construct the adaptive extended Kalman filter algorithm, it is necessary to establish an accurate state space model first. The present study takes the improved second-order RC-PNGV model as the basis and regards the battery's SOC and two polarization voltages, as well as one load integral voltage, as the state vector together. By deriving its nonlinear state equation and observation equation, it provides the core mathematical framework for the AEKF to achieve precise online estimation of SOC.

2.3.1 Construction of state space model

The state space model serves as a bridge connecting the physical characteristics of the battery with the filtering estimation algorithm, and its accuracy and completeness directly determine the estimation precision of SOC and SOP. Based on the improved second-order RC-PNGV equivalent circuit model, the present study constructs a state space model for AEKF.

1. Selection of state variables: The state variables should be capable of comprehensively characterizing the dynamic characteristics of the battery. In the present study, four state variables are selected, which together form the state vector x_k as shown in Equation (13).

$$x_k=[SOC_k,U_{1,k},U_{2,k},U_{C,k}]^T \tag{13}$$

Where SOC_k represents the state of charge of the battery at time k; $U_{1,k}$ and $U_{2,k}$ respectively denote the terminal voltages of the two-stage RC networks, which are used to describe the polarization dynamics at different time scales; $U_{C,k}$ is the capacitor voltage, reflecting the voltage drift caused by continuous charging and discharging. This state vector takes into account both the energy storage state and the internal polarization effect, providing a model basis for high-precision SOP estimation.

2. The establishment of the state equation: The state equation describes the evolution law of the state vector over time. Based on the electrical characteristics and the definition of SOC of the improved second-order RC-PNGV model, the state equation of the system is obtained through discretization by the forward Euler method, as shown in Formula (14).

$$x_{k+1}=f(x_k,I_k)+w_k=\begin{Bmatrix} SOC_k-\dfrac{\eta I_k\Delta t}{Q_n} \\ U_{1,k}e^{-\frac{\Delta t}{\tau_1}}+I_kR_1(1-e^{-\frac{\Delta t}{\tau_1}}) \\ U_{2,k}e^{-\frac{\Delta t}{\tau_2}}+I_kR_2(1-e^{-\frac{\Delta t}{\tau_2}}) \\ U_{c,k}+\dfrac{I_k\Delta t}{C} \end{Bmatrix}+w_k \tag{14}$$

In Equation (14), I_k represents the load current, Δt is the sampling interval, Q_n is the rated capacity, and η is taken as 1. $\tau_1=R_1C_1$ and $\tau_2=R_2C_2$ are the RC time constants, and w_k is the zero-mean Gaussian white noise. The state equation indicates that the SOC is updated through ampere-hour integration, the polarization voltage evolves according to a first-order exponential law, and the PNGV capacitor voltage changes with the integration of the current.

3. Observation equation establishment: The observation equation establishes the connection between the state variables and the directly measurable system output (terminal voltage). According to Kirchhoff's voltage law, the terminal voltage V_k of the battery can be expressed as Equation (15).

$$V_k=\mathrm{OCV}(SOC_k)-I_kR_{\mathrm{equiv}}-U_{1,k}-U_{2,k}-U_{c,k}+v_k \tag{15}$$

In Equation (15), $\mathrm{OCV}(SOC_k)$ is a nonlinear function of SOC, fitted by an 8th-order polynomial to ensure sufficient fitting accuracy for the highly nonlinear OCV-SOC characteristic; R_{equiv} is the series internal resistance. In the present study, the ideal diode is used to distinguish the internal resistance during charging and discharging. During the discharge process, R_{equiv} is set to R_a, whereas during the charge process, it corresponds to R_b. This differentiation improves the voltage simulation accuracy under different working conditions. v_k is zero-mean Gaussian white noise with covariance R, and the observation equation is as shown in Equation (16).

$$V_k=\mathrm{h}(x_k,I_k)+v_k \tag{16}$$

Here, the nonlinear function $\mathrm{h}(\cdot)$ includes the nonlinear mapping of $\mathrm{OCV}(SOC)$ and the switching logic of internal resistance.

2.3.2 Noise adaptive estimation and update mechanism

In actual operation, the battery process noise and observation noise vary dynamically with working conditions, temperature, and aging status. However, the traditional Extended Kalman Filter (EKF) employs a fixed noise covariance, which makes it difficult to describe the time-varying characteristics of the system and may lead to a decline in estimation accuracy or even filter divergence. To address this issue, the present study introduces a noise adaptive update mechanism into the FAP-AEKF framework. By using the filter innovation information, the statistical characteristics of the noise are estimated and corrected online, thereby enhancing the robustness and accuracy of the SOC estimation. The innovation is defined as the difference between the actual observation and the predicted observation, and its calculation is shown in Equation (17).

$$v(k)=v_{\mathrm{meas}}(k)-v_{\mathrm{pred}}(k) \tag{17}$$

Among them, $v_{\mathrm{meas}}(k)$ represents the actual terminal voltage at time k, while $v_{\mathrm{pred}}(k)$ is the predicted terminal voltage calculated based on the state prediction value and the measurement model. To dynamically estimate the covariance matrix of the observation noise R_k, the present study adopts an adaptive update strategy that combines the forgetting factor with the sliding window. The update formula is given by Equation (18).

$$R_k=(1-d)\cdot R_{k-1}+d\cdot\left(\frac{1}{N_\omega}\sum_{i=k-N_\omega+1}^{k} v(i)^2\right) \tag{18}$$

In the formula, d is the forgetting factor ($0 < d < 1$), which is used to balance the influence of historical information and current new information. It is usually set close to 1 to ensure the smoothness of noise estimation. N_ω is the adaptive window size, which is used to limit the length of recent data involved in the calculation of new information variance, avoiding the interference of outdated information in noise estimation. The noise adaptive mechanism constructed in the present study updates the observation noise covariance R_k online by introducing windowed new information analysis with the forgetting factor, forming a closed-loop regulation. This enables the filter to adaptively adjust the observation weights according to the changes in the working conditions, thereby

suppressing interference and accelerating convergence. In this framework, the process noise covariance Q_k is offline optimized during the parameter identification stage and remains constant to ensure the stability of the state evolution. In contrast, only the observation noise covariance R_k is adaptively updated online. This strategy effectively balances the confidence between the model prediction and measurement data, thereby improving the state estimation robustness and accuracy of FAP-AEKF under time-varying conditions.

2.4 Multi-constraint State of Power Estimation Framework

2.4.1 Voltage, current, and State of Charge constraint modeling

The peak power capacity of a battery is not a fixed value but rather the maximum rechargeable and dischargeable power within a specific time scale, while ensuring safety and lifespan. This capacity is strictly limited by various physical and chemical constraints. To achieve a precise and reliable online estimation of SOP, the present study constructs a multi-constraint estimation framework that comprehensively considers voltage, current, and state of charge.

1. Voltage Constraint: The voltage constraint is the primary restriction that prevents the battery from overcharging or overdischarging and ensures its operation within the safe voltage range. This constraint stipulates that the battery terminal voltage U_T shall not exceed the set upper and lower limits after the end of a pulse with a duration of L (in seconds). For the discharge process, the terminal voltage shall not be lower than the minimum allowable value $U_{\min}$; for the charging process, the terminal voltage shall not be higher than the maximum allowable value $U_{\max}$. Its mathematical model can be expressed as Formula (19) and Formula (20).

$$U_T(k+L)\geq U_{\min} \tag{19}$$

$$U_T(k+L)\leq U_{\max} \tag{20}$$

Based on the battery model established in the present study, the terminal voltage U_T is a function of SOC, polarization voltages U_1, U_2, load voltage U_c, and current I. At time k, assuming a constant current I is applied for the next L seconds, the predicted terminal voltage after L seconds can be derived from the state space equation of the model. Taking discharge as an example, its terminal voltage prediction model is Equation (21).

$$\begin{aligned} U_T(k+L)=&OCV(SOC(k+L))-I\cdot R_a-U_1(k)\cdot e^{-L/(R_1C_1)}-U_2(k)\cdot e^{-L/(R_2C_2)} \\ &-U_c(k)-\frac{I\cdot L}{C}-I\cdot R_1(1-e^{-L/(R_1C_1)})-I\cdot R_2(1-e^{-L/(R_2C_2)}) \end{aligned} \tag{21}$$

Equation (21) takes into account the variation of OCV with SOC, the instantaneous voltage drop of the ohmic internal resistance, the transient and steady-state responses of the polarization voltages of the two RC links, as well as the cumulative effect of the load capacitance voltage. By setting $U_T(k+L)=U_{\min}$, the maximum continuous discharge current $I_{\text{discharge,voltage}}$ that satisfies the discharge voltage constraint can be inversely solved. The principle for solving the charging constraint is similar, but the internal resistance R_b corresponding to charging needs to be considered.

2. Current Constraint: The current constraint is directly determined by the BMS or the hardware capabilities of the battery itself (such as connectors, cells), aiming to prevent thermal runaway or permanent damage caused by excessive current. This constraint is typically expressed as an absolute upper limit that is independent of the

time scale L. Its mathematical expressions are given by equations (22) and (23).

$$I \leq I_{\text{discharge,max}} \tag{22}$$

$$I \geq -I_{\text{charge,max}} \quad (I_{\text{charge}} < 0) \tag{23}$$

In these inequalities, $I_{\text{discharge,max}}$ and $I_{\text{charge,max}}$ represent the absolute values of the maximum allowable charging and discharging currents. In the SOP estimation, this constraint serves as a hard cutoff condition to ensure that the calculated peak current does not exceed the hardware safety limit.

3. SOC Constraint: The SOC constraint represents the "energy limit" of the battery, preventing it from being damaged due to excessive charging and discharging or triggering safety risks. This constraint stipulates that after the pulse time L ends, the SOC of the battery must remain within a reasonable range. According to the amper-hour integration method, the SOC after L seconds under a constant current I can be predicted as formula (24).

$$SOC(k+L) = SOC(k) - \frac{I \cdot L}{Q_{\text{nominal}} \times 3600} \tag{24}$$

Among them, Q_{nominal} represents the rated capacity of the battery (Ah). Therefore, the maximum current that satisfies the SOC constraint can be derived: under the discharge SOC constraint, to ensure that $SOC(k+L) \geq SOC_{\text{min}}$, the maximum discharge current must meet formula (25).

$$I_{\text{discharge,soc}} = \frac{(SOC(k) - SOC_{\text{min}}) \cdot Q_{\text{nominal}} \times 3600}{L} \tag{25}$$

Under the constraint of charging SOC, to ensure that $SOC(k+L) \leq SOC_{\text{max}}$, the maximum charging current must satisfy formula (26), and the result is a negative value.

$$I_{\text{charge,soc}} = \frac{(SOC_{\text{max}} - SOC(k)) \cdot Q_{\text{nominal}} \times 3600}{L} \tag{26}$$

Ultimately, the peak current of the battery at a specific time and for a specific duration L is the most stringent of the three constraints, as determined by the above formulas (27) and (28).

$$I_{\text{Peak,discharge}} = min(I_{\text{discharge,voltage}}, I_{\text{discharge,soc}}, I_{\text{discharge,max}}) \tag{27}$$

$$I_{\text{Peak,charge}} = max(-I_{\text{charge,voltage}}, -I_{\text{charge,soc}}, -I_{\text{charge,max}}) \tag{28}$$

Through this collaborative decision-making mechanism, this framework ensures that the SOP estimation results always remain within the safe zone defined jointly by voltage, current, and SOC, providing a crucial guarantee for the optimized management and efficient application of the battery.

2.4.2 Multi-time-scale Peak Power Prediction

Based on the dynamic characteristics of the improved second-order RC-PNGV model and the state variables estimated by the AEKF online algorithm, a multi-time-scale SOP prediction framework is constructed to adapt to the differentiated power demands of the battery power supply under different operating conditions. This framework covers short, medium, and long time-scale scenarios. By introducing equivalent internal resistances that distinguish charging and discharging characteristics and multiple safety constraints, the power prediction is

more in line with the actual operating state. In the calculation of the maximum current, the state variables such as SOC, dual polarization voltage, and capacitor voltage are comprehensively considered, and the nonlinear mechanism of OCV, polarization attenuation, and energy loss are coupled to achieve multi-physical quantity collaborative modeling. The prediction process is supported by optimizing parameter identification and adaptive filtering, and each link forms a linkage error suppression mechanism to ensure the safety and engineering applicability of the SOP prediction. The overall research idea and technical route of the present study are shown in the figure below.

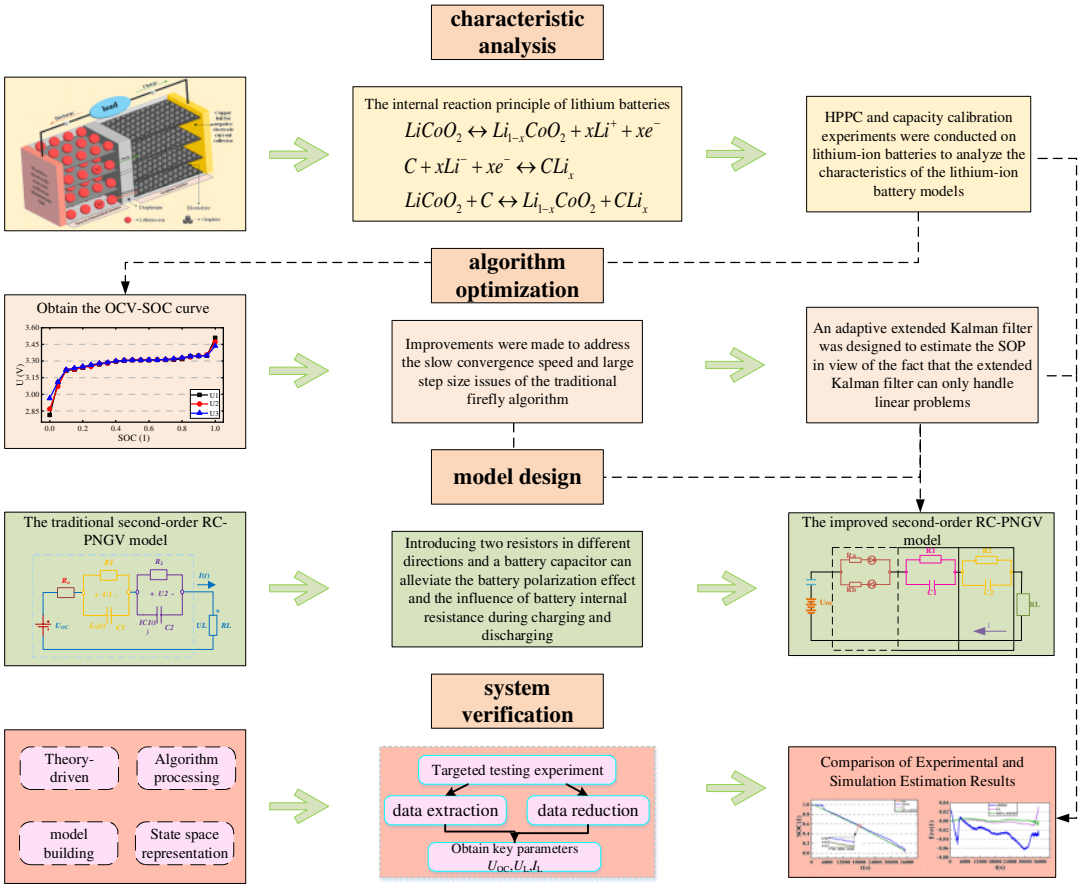


Figure 7. SOP estimation technical route

This flowchart illustrates the overall process of SOP estimation, from experimental data to model establishment, parameter identification, state estimation, and ultimately achieving multi-time-scale SOP prediction.

3 Experimental analysis

To verify the effectiveness of the FAP-AEKF method proposed in the present study in the estimation of the cell state of a ternary lithium-ion battery, this chapter first sets up an experimental testing platform, and provides a detailed description of the used batteries and related testing equipment; subsequently, based on the constructed battery model, SOP estimation experiments are carried out under complex testing conditions and different temperature environments to verify the performance of the FAP-AEKF method; by comparing the experimental

results with the estimation results of the traditional algorithm before improvement, the effectiveness of the proposed algorithm is further confirmed.

3.1 Experimental Design and Data Processing

To verify the effectiveness of the SOP estimation algorithm, this study established a high-rate power battery testing platform. Through presetting working conditions on the upper computer and real-time monitoring, combined with precise temperature control in high and low temperature constant temperature chambers, complex working condition tests were conducted on the ternary lithium-ion battery. The schematic diagram of the experimental platform is shown in Figure 8.

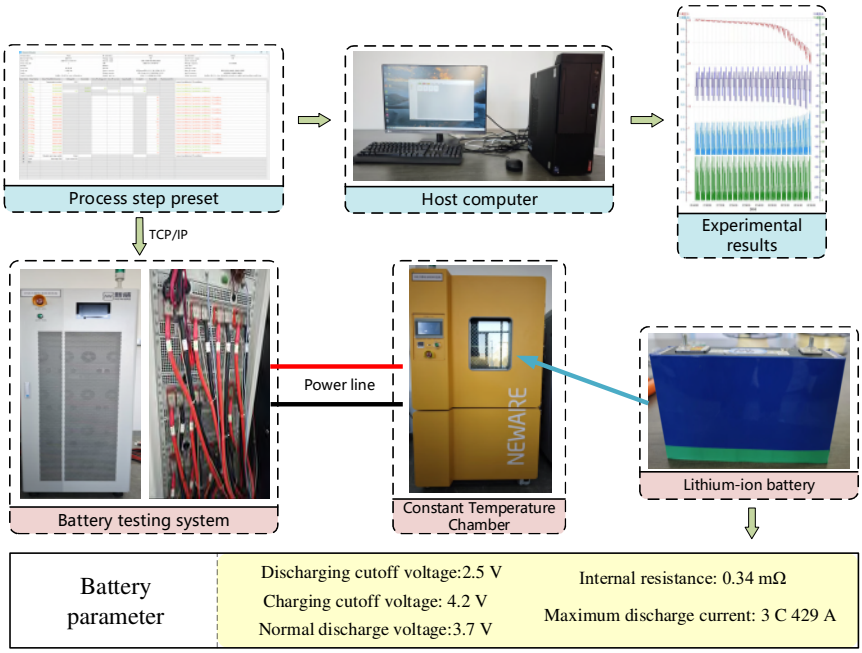


Figure 8. 70143 Type Lithium-ion Battery Experiment Platform

This study took the 70143 type ternary lithium-ion battery as the test object and conducted a series of typical dynamic condition experiments, such as HPPC test, Dynamic Stress Test (DST), and Beijing Bus Dynamic Stress Test (BBDST) under three typical temperature environments of 15℃, 25℃, and 35℃. These test conditions cover multiple characteristics, such as strong pulse discharge, medium dynamic response, and stable load operation, which can comprehensively characterize the electrochemical response mechanism of ternary lithium-ion batteries under different temperature conditions and complex dynamic conditions.

3.2 Parameter identification of the improved second-order RC-PNGV model

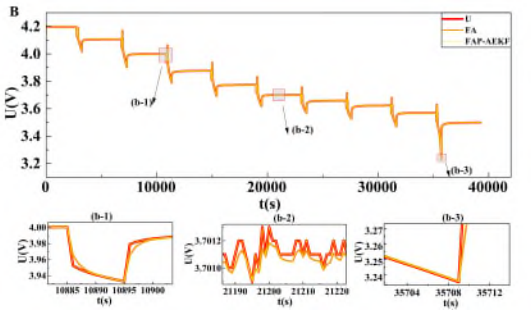
The second-order RC-PNGV model is improved by introducing separate internal resistances for charging and discharging and PNGV capacitance to differentially characterize the polarization characteristics during charging and discharging and to represent the capacity-related dynamic response. Parameter identification takes the weighted deviation between the model output and the measured voltage and SOC as the fitness objective and uses FAP for offline optimization. To balance the observation accuracy and state estimation reliability, the fitness function is constructed as a weighted sum of the RMSE, with weights assigned as 0.7 for the voltage error and 0.3 for the SOC error. This algorithm generates a population within the preset physical constraints and efficiently

searches for the optimal parameters through parallel computing and a global optimization mechanism, combined with the state estimation error provided by AEKF. The identified parameter set has both model structure adaptability and actual operating condition consistency, laying a reliable model foundation for subsequent high-precision SOP estimation.

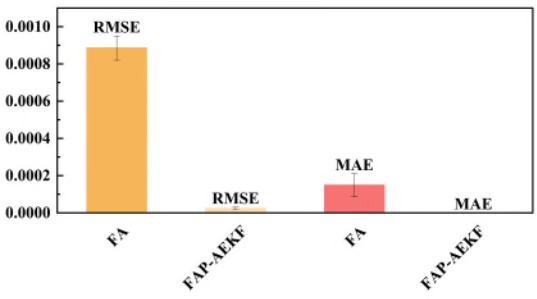
3.3 Voltage fitting under HPPC conditions

To enable the AEKF algorithm to handle the parameter drift of the battery during actual operation and the changes in multiple environmental conditions, the present study uses the FAP algorithm to identify multiple sets of HPPC data at typical temperature points such as 15℃, 25℃, and 35℃ in the offline stage. These high-precision model parameters identified are used as the benchmark mapping table for the online estimation of AEKF, and are dynamically called based on the measured temperature. On this basis, AEKF corrects the system residuals caused by the fluctuation of working conditions through its noise adaptive update mechanism in real time, thus ensuring that even when there is a slight drift in parameters, the SOC estimation still has extremely high physical consistency and robustness.

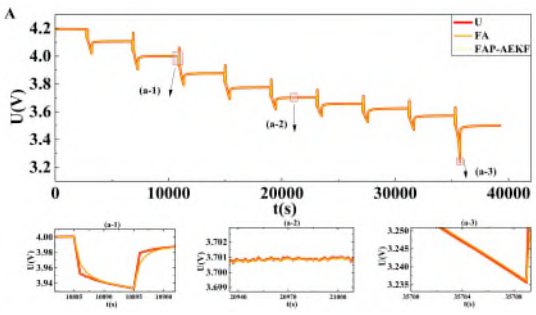
The voltage fitting effect is the core indicator for verifying the effectiveness of the improved second-order RC-PNGV model and the FAP-AEKF algorithm. In this subsection, based on the test data under the HPPC operating condition, by comparing the voltage fitting results of the improved second-order RC-PNGV model combined with the traditional firefly algorithm and the FAP-AEKF algorithm respectively, and considering the quantization indicators such as the RMSE and the mean absolute error (MAE) of the voltage, a systematic analysis is carried out on the voltage fitting performance of the individually improved model and the combination of the improved model and the improved algorithm. Figure 9 shows the voltage fitting analysis comparison under HPPC conditions at various temperatures.

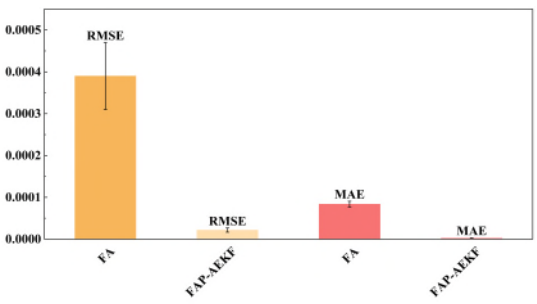


(a) Voltage fitting under HPPC conditions at 15℃



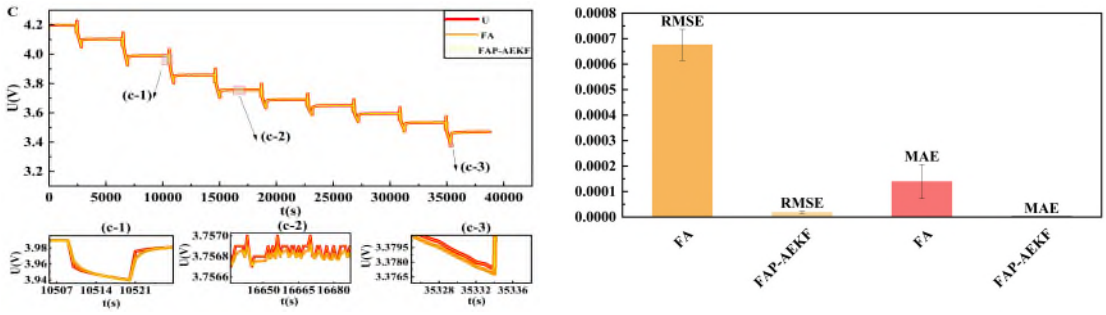
(b) Comparison of voltage fitting errors at 15℃





(c) 0Voltage fitting under HPPC conditions at 25℃

(d) Comparison of voltage fitting errors at 25℃



(e) Voltage fitting under HPPC conditions at 35℃

(f) Comparison of voltage fitting errors at 35℃

Figure 9. Voltage fitting under HPPC conditions at various temperatures

From the voltage fitting curves of HPPC conditions at 15℃, 25℃, and 35℃ presented in Figures 9(a), (c), and (e), it can be seen that when the traditional FA is combined with the improved second-order RC-PNGV model, the voltage fitting accuracy is already at a relatively high level. Meanwhile, the voltage deviation introduced by the battery polarization effect has been significantly suppressed, and the maximum RMSE of the voltage within the entire temperature range does not exceed 0.0009.

Further combining the error comparison results in Figures 9(b), (d), and (f), it can be found that when the improved FAP-AEKF algorithm is jointly solved with the improved second-order RC-PNGV model, the overall error of voltage fitting is further compressed, with the maximum RMSE reduced to below 0.00002. At the same time, the fluctuation range of the error under different temperature conditions is also significantly narrowed. To more intuitively highlight the performance advantages of the FAP-AEKF algorithm, Table 1 lists the specific error quantification data of the two schemes under each temperature condition.

Table 1. Comparison and analysis of voltage fitting errors under HPPC conditions at various temperatures

Type of error	Temperature	Algorithm name	Error magnitude
RMSE	15℃	FA	0.00089
		FAP-AEKF	0.000023
	25℃	FA	0.00039
		FAP-AEKF	0.000022
	35℃	FA	0.00068
		FAP-AEKF	0.000018
MAE	15℃	FA	0.00015
		FAP-AEKF	0.00000052
	25℃	FA	0.000084
		FAP-AEKF	0.0000031
	35℃	FA	0.00014
		FAP-AEKF	0.0000026

Table 1 results show that the FAP-AEKF algorithm, compared with the traditional FA scheme, has achieved a significant reduction in voltage fitting error by several orders of magnitude, with both RMSE and MAE controlled at extremely low levels. This scheme has significantly narrowed the error fluctuation within the full temperature range of 15℃ to 35℃, demonstrating the precise characterization of the charging and discharging polarization characteristics by the improved model and the strong robustness of the FAP-AEKF algorithm. This provides a reliable voltage data foundation for subsequent high-precision state estimation and SOP prediction.

3.4 SOC fitting under DST conditions

DST for electric vehicles is a type of road simulation test method that mimics typical driving conditions such as steady-state driving, acceleration, deceleration, and braking. For lithium-ion battery systems with a ternary cathode, the dynamic changes in the vehicle's operating state directly regulate the battery's power supply mode to meet the power output requirements at different driving stages. Conducting battery performance tests based on DST conditions not only quantitatively verifies the accuracy of the algorithm but also effectively assesses its practicality and long-term stability in real bus driving scenarios. This study focuses on the on-board application scenarios of ternary lithium-ion batteries and constructs an experimental process under DST conditions, as shown in Figure 10.

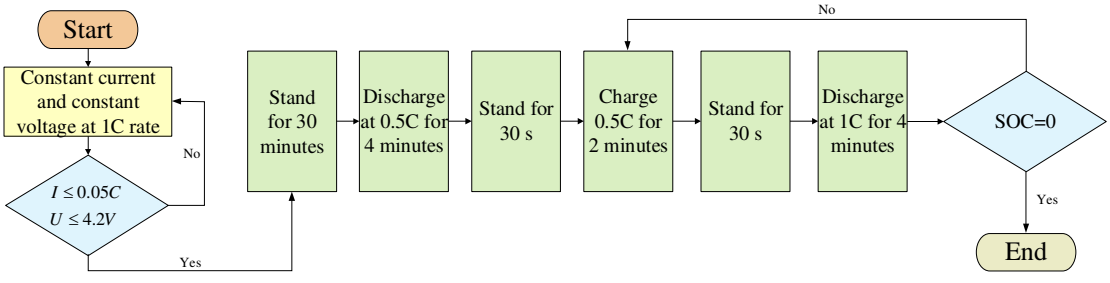
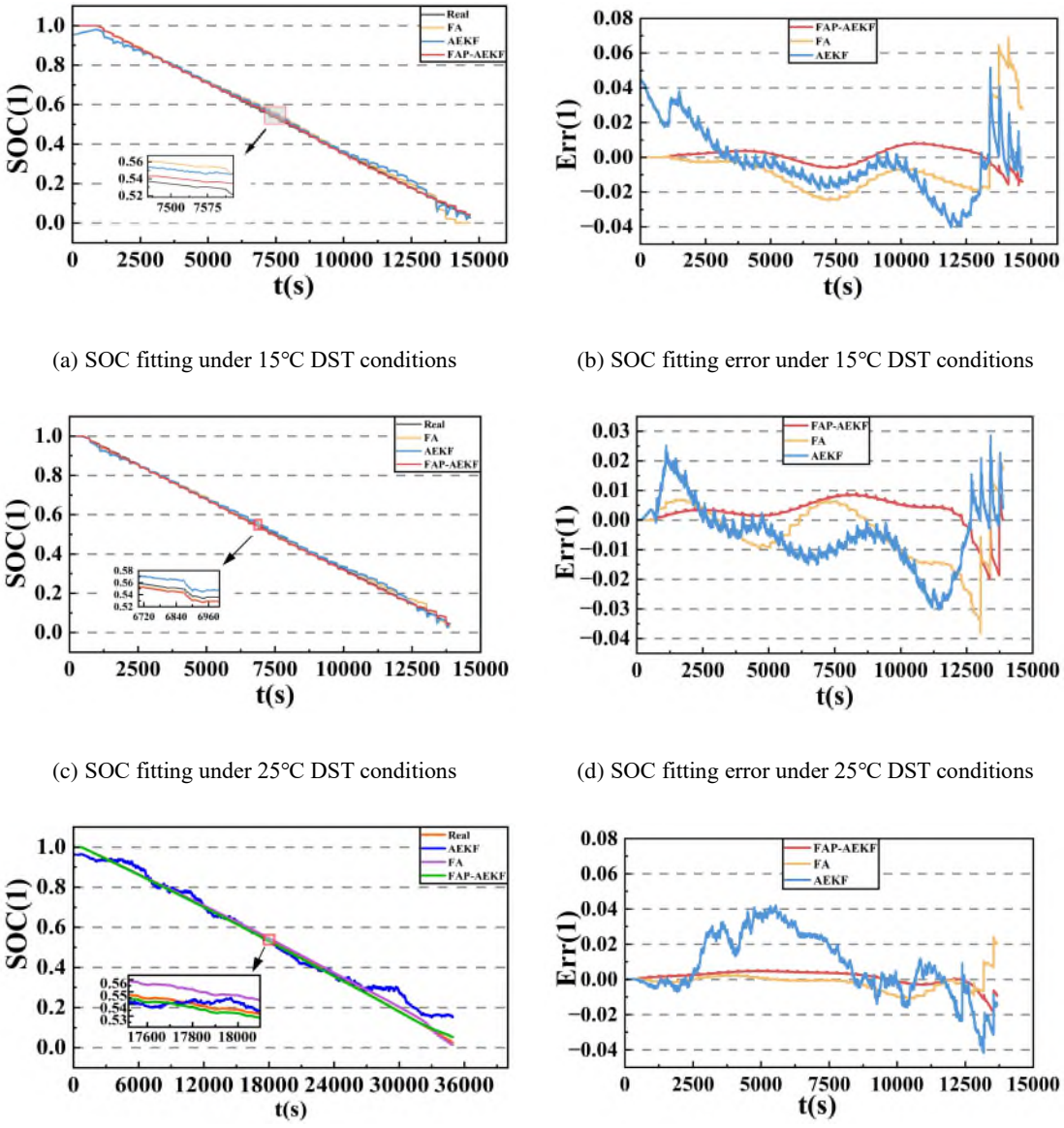


Figure 10. Experimental procedure of targeted DST for ternary lithium batteries

Figure 10 simulates the actual operation state of electric vehicles by regulating the discharge rate and the duration of charging and discharging. Based on the experimental data of DST conditions at three temperatures of 15℃, 25℃, and 35℃, the high accuracy of the proposed FAP-AEKF algorithm in estimating SOC is verified. Meanwhile, by comparing the estimation results of the FA algorithm, the AEKF algorithm, and the FAP-AEKF algorithm, the effectiveness of the proposed algorithm is further confirmed. The SOC estimation results under DST conditions are shown in Figure 11.



(a) SOC fitting under 15℃ DST conditions

(b) SOC fitting error under 15℃ DST conditions

(c) SOC fitting under 25℃ DST conditions

(d) SOC fitting error under 25℃ DST conditions

(e) SOC fitting under 35℃ DST conditions

(f) SOC fitting error under 35℃ DST conditions

Figure 11. SOC fitting effect of DST condition at three temperatures

As shown in Figure 11, at 15℃, 25℃, and 35℃, the fitting error of the AEKF algorithm fluctuates significantly. Although the FA algorithm combined with the improved second-order RC-PNGV model makes the fitting curve closer to the real value and improves the error, it is still relatively large. The SOC fitting curve of the FAP-AEKF algorithm combined with the improved second-order RC-PNGV model has the best fitting degree with the real value, and the error fluctuation is the smallest. Moreover, during the dynamic transition stage of the

working condition start and stop, its error is significantly lower than that of the AEKF algorithm. This not only demonstrates the high-precision characteristics of the FAP-AEKF algorithm but also further confirms the effectiveness of the improved model. Figure 12 shows a detailed comparison of the errors of the three algorithms at each temperature.

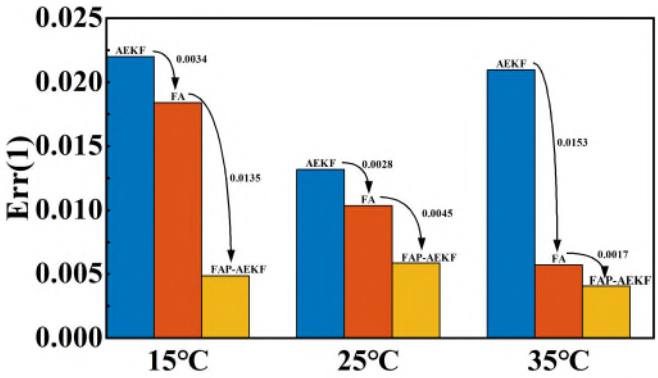


Figure 12. Comparison of SOC fitting errors under three temperature conditions of DST

At 15℃, the error of FAP-AEKF is 0.0153 lower than that of AEKF and 0.0045 lower than that of FA; at 25℃, it is 0.0135 lower than AEKF and 0.0034 lower than FA; at 35℃, it is 0.020 lower than AEKF and 0.0045 lower than FA. It can be seen that the FAP-AEKF algorithm can significantly reduce the SOC estimation error throughout the entire temperature range. Combined with the improved second-order RC-PNGV model, its robustness is stronger, fully verifying the optimization effect of the algorithm and providing strong support for the subsequent high-precision estimation of SOP.

3.5 SOC fitting under BBDST conditions

To provide a reliable basis for the subsequent multi-constraint SOP estimation, the accuracy of the proposed SOC estimation method based on FAP-AEKF was first verified based on the experimental data collected under the BBDST conditions (15℃, 25℃, 35℃). By comparing the SOC estimation results of the AEKF algorithm, the FA algorithm, and the proposed FAP-AEKF algorithm, the effectiveness of the algorithm in this study was further verified.

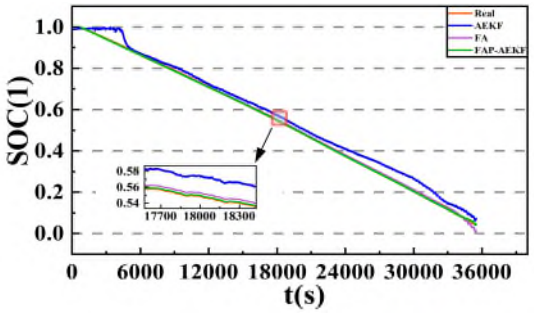
This section first elaborates on the BBDST conditions and their operational characteristics. Based on this test standard, an experimental scheme was formulated, and an experimental platform was built to conduct tests on ternary lithium batteries. The specific experimental parameters and operation steps are shown in Table 2.

Table 2. Parameters and Descriptions of BBDST Operating Conditions

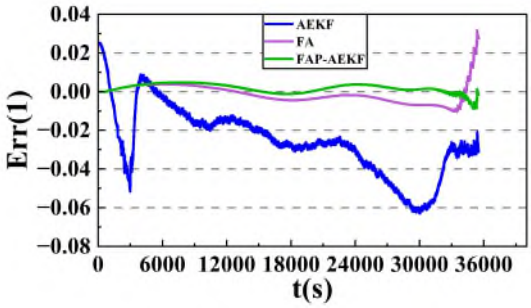
Work steps	P_h(w)	One step (s)	Cumulative(s)	Operating conditions	Work steps	P_h(w)	One step (s)	Cumulative(s)	Operating conditions
1	75	21	21	Getting started	11	9	16	150	Sliding
2	145	12	33	Acceleration	12	-30	6	156	Brake
3	9	16	49	Sliding	13	145	9	165	Acceleration

Work steps	P_h(w)	One step (s)	Cumulative(s)	Operating conditions	Work steps	P_h(w)	One step (s)	Cumulative(s)	Operating conditions
4	-30	6	55	Brake	14	185	6	171	Sudden acceleration
5	75	21	76	Acceleration	15	75	21	192	Acceleration
6	9	16	92	Sliding	16	9	16	208	Sliding
7	-30	6	98	Brake	17	-70	9	217	Brake
8	145	9	107	Acceleration	18	-30	6	229	Brake
9	185	6	113	Sudden acceleration	19	9	71	300	Park the car
10	75	21	134	Acceleration					

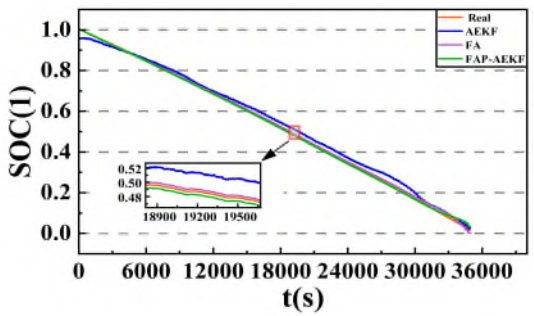
The BBDST operating condition characteristics are based on the actual operation data collection of buses in Beijing and were constructed. Considering that the experimental object is a single ternary lithium-ion battery, the actual operation power is scaled and adjusted to obtain the power parameters suitable for this experimental object (as shown in Table 2). In the table, "single step time" is defined as the duration of each operating condition step, and "cumulative time" is defined as the cumulative value of the duration of each step. As can be seen from 2, the single complete cycle time of the BBDST operating condition is 300 seconds. During the experiment, multiple repeated cycle tests of the BBDST operating condition were conducted on the battery. The SOC estimation results under the BBDST operating condition are shown in Figure 13.



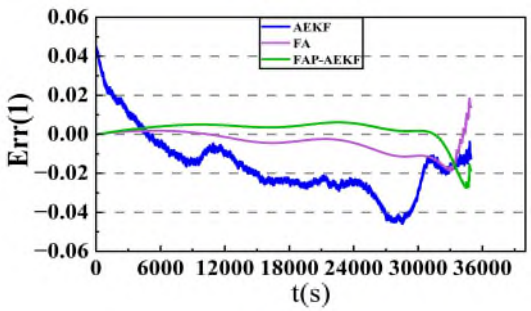
(a) SOC fitting under 15℃ BBDST conditions



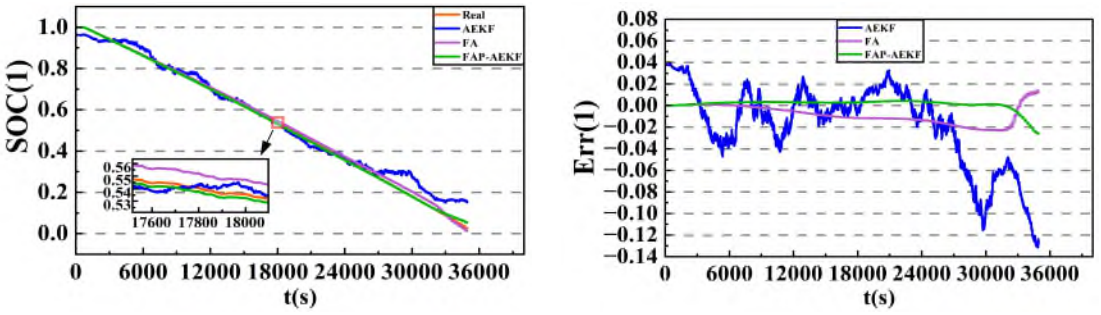
(b) SOC fitting error under 15℃ BBDST conditions



(c) SOC fitting under 25℃ BBDST conditions



(d) SOC fitting error under 25℃ BBDST conditions



(e) SOC fitting under 35℃ BBDST conditions (f) SOC fitting error under 35℃ BBDST conditions

Figure 13. SOC Fitting of BBDST Conditions at Three Temperatures

It can be seen from (b), (d), and (f) in the figure that the traditional AEKF algorithm shows significant fluctuations in the SOC estimation under the BBDST condition, with the maximum error reaching 13.2%. The stability of the FA algorithm, combined with the improved second-order RC-PNGV model, has been enhanced, and the error fluctuation has narrowed. However, the FAP-AEKF algorithm combined with the improved second-order RC-PNGV model performs outstandingly. It can maintain a stable error in the later stage under all temperature conditions, and the maximum errors under the three temperatures do not exceed 2.8%. This fully demonstrates the improvement effect of the improved algorithm on the accuracy and stability of SOC estimation.

3.6 Estimation of multi-constraint SOP

To systematically evaluate the performance of the proposed method in estimating the SOP under typical dynamic conditions, this section conducts SOP charge and discharge power estimation experiments at two typical temperatures of 15℃ and 35℃ based on two dynamic test conditions, namely DST and BBDST, over multiple time scales (30s, 60s, and 180s). The constraint limit values are shown in Table 3 to ensure the battery operates within a safe range.

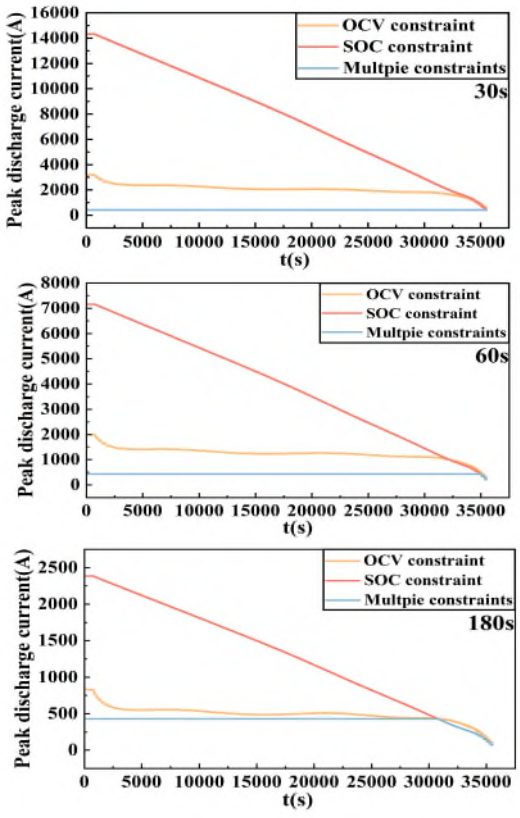
Table 3. Each constraint condition in SOP estimation

parameter	maximum value	least value
SOC limit value	1	0
Current design limit	439A	-143A
Terminal voltage limit	4.2V	2.5V

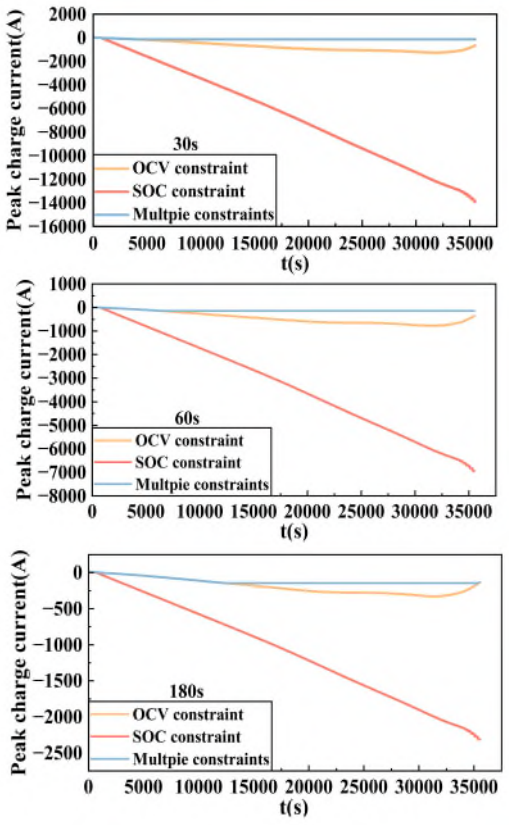
This SOP strictly adheres to the triple safety constraints of voltage, current, and SOC: the SOC limit (0 to 1) prevents overcharging or overdischarging, the designed current limit (-143 to 439 A) avoids thermal runaway, and the terminal voltage limit (2.5 to 4.2 V) ensures a safe operating window. These multiple constraints jointly define the safety operation boundary of the battery and provide the core basis for peak power calculation.

3.6.1 Estimation of SOP charge and discharge power under different temperature BBDST conditions

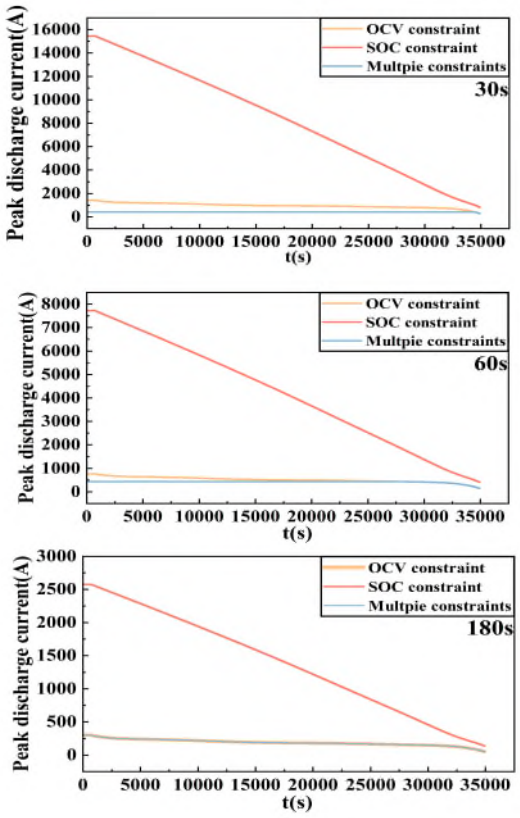
To demonstrate the effectiveness of the FAP-AEKF algorithm in estimating the SOP at different temperatures, experiments were first conducted under the BBDST condition. The experimental results obtained are shown in Figure 14.

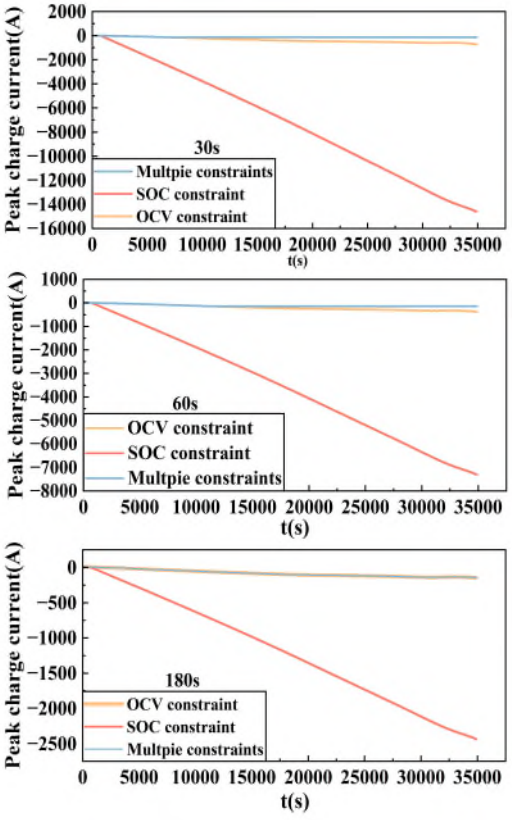


(a) Peak discharge current at 15℃ BBDST operating condition



(b) Peak charging current at 15℃ BBDST operating condition





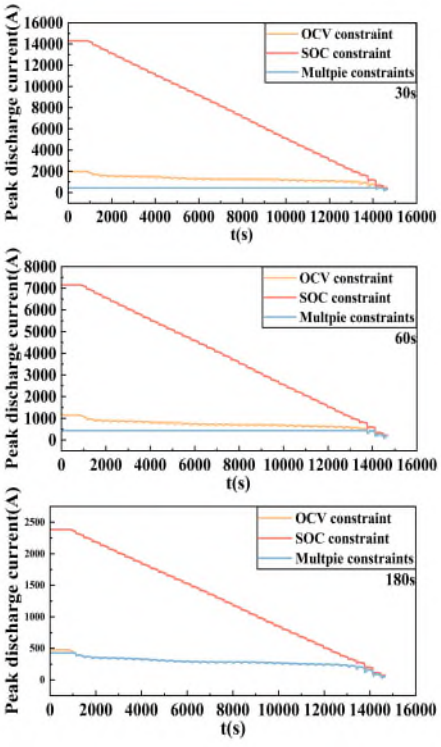
(c) Peak discharge current at 35℃ BBDST operating condition (d) Peak charging current at 35℃ BBDST operating condition

Figure 14. The peak charge and discharge currents under two temperature BBDST operating conditions

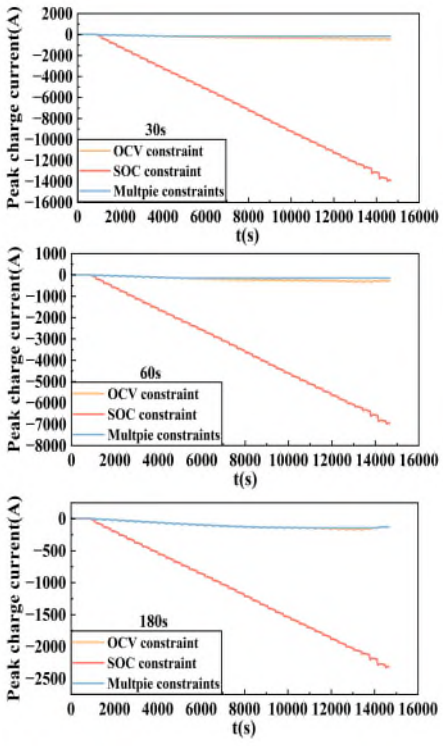
Figure 14 presents the estimated peak charge and discharge current results of the battery under the BBDST condition at two temperatures, 15℃ and 35℃. Generally speaking, the peak charge and discharge capacity of the battery are closely related to the duration of continuous charge and discharge. It is manifested that the shorter the duration, the greater the peak current that can be output. This is mainly because short-term high-rate pulses allow for greater electrode overpotential. The curves of different durations in the figure clearly demonstrate this rule. At the same time, all curves show an overall attenuation trend with the test process (corresponding to the decrease of SOC), and are superimposed with significant local fluctuations, which precisely reflect the dynamic changes in power demand during actual driving stages such as acceleration, coasting, and braking in the BBDST condition. By comparing the curves at different temperatures, it can be seen that the peak current capacity of the battery is generally higher at high temperature (35℃) than at low temperature (15℃), and the curves are smoother. This is due to the fact that high temperature reduces the internal resistance of the battery and alleviates the polarization effect. In addition, the charge and discharge curves show asymmetry in amplitude and shape, intuitively revealing the intrinsic differences in the charge and discharge mechanisms and safety boundaries of the battery.

3.6.2 Estimation of SOP charge and discharge power under different temperature DST conditions

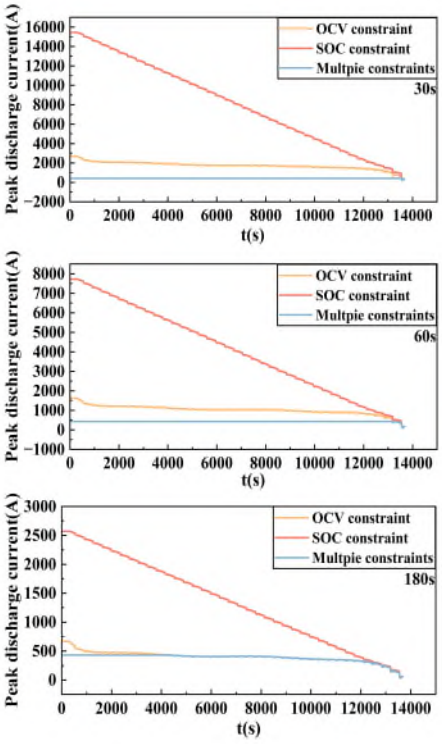
To further verify the effectiveness of the FAP-AEKF algorithm and the improved model, the present study conducted SOP estimation based on the experimental results of the aforementioned DST conditions. The obtained results are shown in Figure 15.



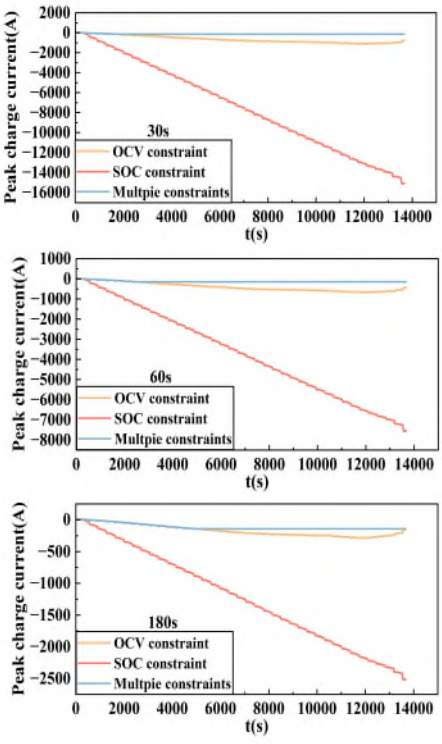
(a) Peak discharge current at 15℃ DST condition



(b) Peak charging current at 15℃ DST conditions



(c) Peak discharge current at 35℃ DST condition



(d) Peak charging current at 35℃ DST conditions

Figure 15. The peak charge and discharge currents under two temperature DST conditions

Figure 15 shows the peak charge and discharge currents at different temperatures under the DST condition. Similar to the BBDST condition, the peak current decreases as the duration increases, and the current at high temperature (35℃) is generally higher than that at low temperature (15℃). The fluctuations in the curves are consistent with the power demand changes under the DST condition. The differences in the shapes of the charge and discharge curves visually reflect the polarization characteristics and safety boundaries of the battery in different directions.

Table 4. Estimation Results of Continuous Peak Charging and Discharging Power

Temperature (℃)	Operating conditions	Charging / Discharging	Duration(s)	MAE(W)
15	DST	Charging	30	16
			60	14
			180	17
		Discharging	30	26
			60	27
			180	23
	BBDST	Charging	30	15
			60	12
			180	15

Temperature (℃)	Operating conditions	Charging / Discharging	Duration(s)	MAE(W)
35	DST	Discharging	30	22
			60	27
			180	28
		Charging	30	15
			60	17
			180	17
		Discharging	30	24
			60	24
			180	25
	BBDST	Charging	30	18
			60	17
			180	16
		Discharging	30	21
			60	22
			180	27

Table 4 results show that under different temperatures and working conditions, the average error of charging and discharging power is relatively small, with charging at approximately 12–18 W and discharging at approximately 21–28 W. Moreover, no significant accumulation was observed as the duration increased. The overall error at 35℃ is lower than or close to that at 15℃, indicating that this method has good consistency and robustness under multiple time scales and temperature variations.

4 Conclusion

As a core component of new energy vehicles, the accurate estimation of the SOP for lithium-ion batteries is of great significance to the safety and reliability of battery management systems. To improve the estimation accuracy of SOP under complex working conditions, the present study proposes a high-precision FAP-AEKF estimation framework, which integrates an improved second-order RC-PNGV model, an FAP, and an AEKF. By introducing differentiated polarization resistance and PNGV capacitor branches, the model's ability to describe the asymmetric polarization characteristics during charging and discharging is significantly enhanced. Meanwhile, the FAP algorithm achieves high-precision identification of model parameters and effectively improves the parameter identification efficiency and convergence performance, providing a reliable model basis for the filtering stage. Experimental results under typical working conditions (HPPC, DST, and BBDST) across a temperature range of 15℃ to 35℃ show that the terminal voltage fitting RMSE of the FAP-AEKF method is less than 0.01 V, and the maximum SOC estimation error does not exceed 2.80%. In multi-time-scale SOP estimation, the average error of peak power is controlled within 17 W for the short-term scale and does not exceed 28 W for the long-term scale, demonstrating a significant accuracy advantage over traditional methods. The research results verify the high accuracy and robustness of the FAP-AEKF framework under multiple working conditions and temperature

variations, providing reliable support for power distribution and safety boundary determination of power batteries. Future research will further expand to the SOP estimation problems of series-parallel battery packs and under aging conditions.

Acknowledgments

The work is supported by the National Natural Science Foundation of China (No. 62173281, 52377217, U23A20651), National Key Research and Development Program (No. 2024YFB2408400), Sichuan Science and Technology Program (No. 24NSFSC0024, 23ZDYF0734, 23NSFSC1436), Dazhou City School Cooperation Project (No. DZXQHZ006), Open Fund Project of State Key Laboratory of Mining Response and Disaster Pre-vention and Control in Deep Coal Mines (No. SKLMRDPC23KF19), Inner Mongolia Energy Strategy Research Center Project (24NYZL07), Graduate Education Teaching Reform Project (24YJG027) and Robert Gordon University.

References

[1] Hou Jie, Yang Qingyin. Lithium Battery SOC Estimation Based on Simplified Model and Adaptive Algorithm [J]. Journal of Engineering Sciences, 2026.

[2] Liu Yuyang, Wang Shunli, Xie Yanxin, et al. Research on lithium-ion battery modeling and SOC estimation based on online parameter identification and improved 2RC-PNGV model [J]. Energy Storage Science and Technology, 2021, 10(06): 2312-2317.

[3] Luo Yutao, Wu Zhiqiang. Online Joint Estimation of Main States of Lithium-ion Batteries Based on DAEKF Algorithm [J]. Journal of South China University of Technology: Natural Science Edition, 2023, 51(1): 84-94.

[4] Wu Chunling, Ma Yao, Chang Zhanhao, et al. High-precision and robust estimation of power state of lithium-ion batteries based on multi-constraint dynamic fusion and SSA-ELM error compensation [J]. Energy Storage Science and Technology, 2025, 14(11): 4309-4320.

[5] Bhattacharya T, Ghosh S. Data driven approach for state-of-charge estimation of lithium-ion cell using stochastic variational Gaussian process [J]. Computers and Electrical Engineering, 2024, 120: 109727.

[6] Bhattacharya T, Ghosh S. Enhancing state of charge estimation accuracy in lithium-ion batteries through adaptive incremental learning under ambient temperature variability [J]. Energy Sources, Part A: Recovery, Utilization, and Environmental Effects, 2025, 47(1): 9413-9434.

[7] Chen C, Li Z, Wei J. Estimation of Lithium-Ion Battery State of Charge Based on Genetic Algorithm Support Vector Regression under Multiple Temperatures [J/OL] 2023, 12(21):4433[10.3390/electronics12214433

[8] Chen C, Zhang Q, Liao W, et al. State of charge estimation for lithium-ion batteries using an adaptive cubature Kalman filter based on improved generalized minimum error entropy criterion [J]. Green Energy and Intelligent Transportation, 2026, 5(1): 100292.

[9] Chen J, Zhang Y, Wu J, et al. SOC estimation for lithium-ion battery using the LSTM-RNN with extended input

and constrained output [J]. Energy, 2023, 262: 125375.

[10] Cui Z, Kang L, Li L, et al. A combined state-of-charge estimation method for lithium-ion battery using an improved BGRU network and UKF [J]. Energy, 2022, 259: 124933.

[11] D O P, Babu P S, V I, et al. Enhanced SOC estimation of lithium ion batteries with RealTime data using machine learning algorithms [J]. Scientific Reports, 2024, 14(1): 16036.

[12] Deng H, Liu L, Fang J, et al. A novel improved whale optimization algorithm for optimization problems with multi-strategy and hybrid algorithm [J]. Mathematics and Computers in Simulation, 2023, 205: 794-817.

[13] Zheng B, Deng Z, Luo Z, et al. A comprehensive review of lithium-ion battery modelling research and prospects: in-depth analysis of current research and future directions [J]. Applied Energy, 2025, 401: 126688.

[14] Zhou Z, Zhan M, Wu B, et al. A novel adaptive unscented kalman filter algorithm for SOC estimation to reduce the sensitivity of attenuation coefficient [J]. Energy, 2024, 307: 132598.

[15] Dong S, Zhang X, Huang L, et al. State of Power Online Estimation Considering Inconsistency for Series-Connected Lithium Titanate Battery Packs [J]. IEEE Transactions on Industrial Electronics, 2025, 72(12): 13322-13333.

[16] Liu Ying, Sun Bingxiang, Zhao Xinzhe, et al. Joint Estimation of SOC/SOP of Lithium-ion Batteries in Wide Temperature Range Based on Electrothermal Coupling Model [J]. Energy Storage Science and Technology, 2024, 13(09): 3030-3041.

[17] Wang S, Wu Y, Zhou H, et al. Improved particle swarm optimization-adaptive dual extended Kalman filtering for accurate battery state of charge and state of energy joint estimation with efficient core factor feedback correction [J]. Energy, 2025, 322: 135686.

[18] Xiao F, Li C, Fan Y, et al. State of charge estimation for lithium-ion battery based on Gaussian process regression with deep recurrent kernel [J]. International Journal of Electrical Power & Energy Systems, 2021, 124: 106369.

[19] Yu C, Zhu J, Liu W, et al. Co-estimation of state-of-charge and state-of-temperature for large-format lithium-ion batteries based on a novel electrothermal model [J]. Green Energy and Intelligent Transportation, 2024, 3(4): 100152.

[20] Hao X, Wang S, Fan Y, et al. A novel least squares support vector machine-particle filter algorithm to estimate the state of energy of lithium-ion battery under a wide temperature range [J]. Journal of Energy Storage, 2024, 89: 111820.

[21] Yu K, Zhang K, Zhong Y, et al. Fractional-order modeling and parameter estimation of lithium-ion battery via multi-strategy and mean factor differential evolution [J]. Measurement, 2025, 246: 116721.

[22] Zhang C, Zhao H, Xu Y, et al. State of charge accurate estimation of lithium-ion batteries based on augmenting observation dimension estimator over wide temperature range [J]. Energy, 2025, 316: 134515.

[23] Fan X, Feng H, Yun X, et al. SOC estimation for lithium-ion battery based on AGA-optimized AUKF [J]. Journal

of Energy Storage, 2024, 75: 109689.

[24] Feng R, Wang S, Yu C, et al. High Precision State of Health Estimation of Lithium-ion Batteries Based on PSO-LSSVM AdaBoost Model; proceedings of the 2024 IEEE 25th China Conference on System Simulation Technology and its Application (CCSSTA), F 21-23 July 2024, 2024 [C].

[25] Gao G, Dong G, Lou Y, et al. Physics-Informed Data-Driven Power Capacity Prediction of Lithium-Ion Battery Against Various Temperatures [J]. IEEE Transactions on Intelligent Transportation Systems, 2025, 26(6): 8670-8681.

[26] Guo R, Hu C, Shen W. Battery Peak Power Assessment Under Various Operational Scenarios: A Comparative Study [J]. IEEE Transactions on Transportation Electrification, 2025, 11(1): 2489-2503.

[27] Ho K-C, Khanh D N, Hsueh Y-F, et al. Deep Learning Approach for Equivalent Circuit Model Parameter Identification of Lithium-Ion Batteries [J/OL] 2025, 14(11):2201[10.3390/electronics14112201

[28] Huang B, Li H, Sun J, et al. Robust SOC estimation for lithium-ion batteries: Combination of GRU and FOMIAUKF approach with an improved state transition matrix [J]. Energy, 2025, 328: 136429.

[29] Jafari S, Byun Y-C. AI-driven state of power prediction in battery systems: A PSO-optimized deep learning approach with XAI [J]. Energy, 2025, 331: 136764.

[30] Kuai X, Ren J-H, Wang B-C, et al. Large language model-enhanced Bayesian optimization for parameter identification of lithium-ion batteries [J]. Journal of Energy Storage, 2025, 135: 118198.

[31] Li H, Jia H, Xiao P, et al. Research Progress on State of Charge Estimation Methods for Power Batteries in New Energy Intelligent Connected Vehicles [J]. Energies, 2025, 18(9): 2144.

[32] Li R, Li K, Liu P, et al. Research on Multi-Time Scale SOP Estimation of Lithium–Ion Battery Based on H∞ Filter [J/OL] 2023, 9(4):191[10.3390/batteries9040191

[33] Majewski K, Żugaj M. Deep Q-Network-Based Adaptive Noise Covariance Estimation for Kalman Filter Tuning; proceedings of the 2025 IEEE Statistical Signal Processing Workshop (SSP), F 8-11 June 2025, 2025 [C].

[34] Mohamed M a A, Yu T F, Ramsden G, et al. Advancements in parameter estimation techniques for 1RC and 2RC equivalent circuit models of lithium-ion batteries: A comprehensive review [J]. Journal of Energy Storage, 2025, 113: 115581.

[35] Nishanth G, Krishnan M M, Parandhaman B, et al. Hardware implementation of EKF based SOC estimate for lithium-ion batteries in electric vehicle applications [J]. Scientific Reports, 2025, 15(1): 15551.

[36] Peng H, Xiao W, Han Y, et al. Multi-strategy firefly algorithm with selective ensemble for complex engineering optimization problems [J]. Applied Soft Computing, 2022, 120: 108634.

[37] Pi J, Da Silva S F, Ozkan M F, et al. Parameter Identification for Electrochemical Models of Lithium-Ion Batteries Using Bayesian Optimization [J]. IFAC-PapersOnLine, 2024, 58(28): 180-185.

[38] Qi Y, Zhao W, Sun X, et al. State estimation of Li-ion batteries via improved second-order RC model [J]. Energy

Reports, 2025, 14: 31-42.

[39] Saban O B, Arslan M A, Serincan M F. Multiphysics modeling of lithium-ion batteries: a novel DRT-enhanced electro-thermal framework [J]. Ionics, 2025, 31(10): 10327-10351.

[40] Schmitt J, Horstkötter I, Bäker B. A novel approach for modelling voltage hysteresis in lithium-ion batteries demonstrated for silicon graphite anodes: Comparative evaluation against established Preisach and Plett model [J]. Journal of Power Sources Advances, 2024, 26: 100139.

[41] Sheikh A M A, Donkers M C F, Bergveld H J. Towards temperature-dependent linear parameter-varying models for lithium-ion batteries using novel experimental design [J]. Journal of Energy Storage, 2025, 119: 116311.

[42] Tian J, Chen C, Shen W, et al. Deep Learning Framework for Lithium-ion Battery State of Charge Estimation: Recent Advances and Future Perspectives [J]. Energy Storage Materials, 2023, 61: 102883.

[43] Wang C, Li R, Cao Y, et al. A hybrid model for state of charge estimation of lithium-ion batteries utilizing improved adaptive extended Kalman filter and long short-term memory neural network [J]. Journal of Power Sources, 2024, 620: 235272.

[44] Wang Q, Gu H, Ye M, et al. State of Charge Estimation for Lithium-Ion Battery Based on NARX Recurrent Neural Network and Moving Window Method [J]. IEEE Access, 2021, 9: 83364-83375.

[45] Wang S, Cao J, Xie Y, et al. A Novel 2-RC Equivalent Model Based on the Self-Discharge Effect for Accurate State-Of-Charge Estimation Of Lithium-Ion Batteries [J]. International Journal of Electrochemical Science, 2022, 17(7): 22072.